Article

Vinculin Force-Sensitive Dynamics at Focal Adhesions Enable Effective Directed Cell Migration

Katheryn E. Rothenberg,[1] David W. Scott,[2] Nicolas Christoforou,[1] and Brenton D. Hoffman[1],*
[1]Department of Biomedical Engineering, Duke University, Durham, North Carolina and [2]Lineberger Comprehensive Cancer Center, UNC Chapel, Chapel Hill, North Carolina

ABSTRACT Cell migration is a complex process, requiring coordination of many subcellular processes including membrane protrusion, adhesion, and contractility. For efficient cell migration, cells must concurrently control both transmission of large forces through adhesion structures and translocation of the cell body via adhesion turnover. Although mechanical regulation of protein dynamics has been proposed to play a major role in force transmission during cell migration, the key proteins and their exact roles are not completely understood. Vinculin is an adhesion protein that mediates force-sensitive processes, such as adhesion assembly under cytoskeletal load. Here, we elucidate the mechanical regulation of vinculin dynamics. Specifically, we paired measurements of vinculin loads using a Förster resonance energy transfer-based tension sensor and vinculin dynamics using fluorescence recovery after photobleaching to measure force-sensitive protein dynamics in living cells. We find that vinculin adopts a variety of mechanical states at adhesions, and the relationship between vinculin load and vinculin dynamics can be altered by the inhibition of vinculin binding to talin or actin or reduction of cytoskeletal contractility. Furthermore, the force-stabilized state of vinculin required for the stabilization of membrane protrusions is unnecessary for random migration, but is required for directional migration along a substrate-bound cue. These data show that the force-sensitive dynamics of vinculin impact force transmission and enable the mechanical integration of subcellular processes. These results suggest that the regulation of force-sensitive protein dynamics may have an underappreciated role in many cellular processes.

INTRODUCTION

Cell migration is a complex, spatiotemporally regulated process that enables cells to move either randomly or in a directed manner in response to biochemical and biophysical cues (1,2). Directed migration is integral to many fundamental biological processes, such as wound healing, morphogenesis, and the immune response, and defects in cell migration are associated with a variety of pathological conditions, such as birth defects, cancer metastasis, and vascular disease (3–6). Efficient cell migration requires the coordinated regulation of cell protrusion driven by actin polymerization in the lamellipodia (7), adhesion to the extracellular matrix (ECM) mediated by integrin-based multiprotein complexes termed "focal adhesions" (FAs) (8), and force generation via the actomyosin cytoskeleton through actin polymerization or myosin activity (9,10). However, the molecular mechanisms mediating the coordinated regulation, and particularly the mechanical integra-

tion, of these subcellular structures during cell migration are incompletely understood.

As FAs mediate the mechanical connections between the ECM and the force-generating actomyosin cytoskeleton, these structures play a key role in the coordination of subcellular processes during cell migration (1,11). For cells to efficiently migrate, FAs must perform two seemingly opposed mechanical functions: stably transmit large forces to the ECM to provide the driving force for forward motion at the leading edge of the cell, and undergo force-induced rearrangements to enable translocation of the cell body. Biologically, the regulation of these dynamics is often explained in terms of two distinct phenomena: as force-sensitive molecular clutches (12–15) or as force-induced FA growth (often referred to as "adhesion strengthening" (16–19)). The molecular-clutch models mostly focus on the ability of force to destabilize or reinforce the physical connections between FA proteins, commonly referred to as "slip" or "catch" bonds (12,15,20,21). Force-induced growth models tend to focus on the ability of mechanical loading to cause conformation changes in proteins that induce recruitment of proteins to FAs (22–24). Interestingly,

recent models have proposed that both processes interact to mediate mechanosensing (25,26).

Efforts to identify the key proteins governing mechanical regulation of FA dynamics have primarily focused on talin and vinculin. Both proteins are critical to maintaining cell spread area, stable FAs, and engagement with the actin cytoskeleton (27–30). Additionally, both proteins undergo conformation regulation, where the closed conformation is mediated by a strong interaction between the N-terminal head domain and C-terminal domains (31–33), and the open conformation is thought to mediate formation of stable load-bearing connections within FAs (34,35). Talin in the open conformation binds directly to integrins and F-actin and bears substantial mechanical load (36,37). Vinculin in the open conformation links talin to actin and also bears substantial mechanical load (29,30,38–41). However, recent evidence has revealed that closed vinculin still localizes to FAs (41,42), indicating that the open conformation of vinculin is not required for FA localization. Despite demonstration of distinct localization of open and closed vinculin at the FA (42), it is unclear how these states are regulated or their importance in FA function.

Interactions between vinculin and talin are highly regulated, and particularly sensitive to mechanical loading. Applying sufficient force to talin exposes cryptic vinculin binding sites, thought to be a primary mechanism for recruitment and stabilization of open vinculin at the FA (43–45), although recent evidence indicates that phosphorylated paxillin might recruit closed vinculin to the distal tip of the FA (42). Furthermore, activated vinculin stabilizes the open conformation of talin and induces interactions between talin and actin (28,29,46), reinforcing the mechanical linkage between integrins and the actomyosin cytoskeleton. Based on these results, it has been suggested that either talin, vinculin, or the interaction of talin and vinculin, is the key component of the molecular clutch or the crucial element in force-induced FA strengthening (15,25,30,45,47). Further progress requires a greater understanding of how force affects talin and vinculin dynamics and interactions in living cells.

Although the exact molecular mechanisms are still under investigation, it is clear that applied force affects the turnover dynamics of proteins with FAs. Collectively, we refer to any of these processes as "force-sensitive protein dynamics." Previous efforts to probe force-sensitive protein dynamics in living cells have largely relied on fluorescence recovery after photobleaching (FRAP) in conjunction with indirect manipulations of mechanical forces, including inhibition of the actomyosin cytoskeleton or different rigidity substrates (40,47–51). Vinculin turnover dynamics are slowed in response to the increased activity of the actomyosin cytoskeleton, stiffer substrates, and local increases in traction force generation, indicating that actomyosin-generated forces stabilize vinculin at the FA, but the exact mechanism is unclear. For instance, this stabilization could

be explained by force-induced changes in vinculin-talin or vinculin-actin bond dynamics or, alternatively, by force-induced modulation of structural elements that stabilize vinculin at the FA.

To elucidate the mechanisms mediating the observed force-induced stabilization of vinculin at FAs, we developed a combination of existing techniques for probing force-sensitive protein dynamics in living cells and applied the technique to vinculin. The key advance of the technique over previous efforts is the use of Förster resonance energy transfer (FRET)-based biosensors that enable direct measurements of the forces experienced by vinculin and do not rely on manipulations that globally affect cell contractility. With this new, to our knowledge, approach, we observe different forms of vinculin force-sensitive dynamics, likely corresponding to distinct mechanical states of the protein. Furthermore, a particular, force-stabilized, state is required for the coordination of subcellular processes and effective directed cell migration. Together, these data suggest that a variety of classes of mechanical clutches, with distinct physical properties, form to enable distinct force-sensitive responses in FAs.

MATERIALS AND METHODS

Cell culture

Mouse embryonic fibroblasts lacking vinculin (Vinc −/− MEFs), along with cells derived from wild-type littermate controls (WT MEFs), were generously provided by Drs. Ben Fabry, Wolfgang Goldman, and Wolfgang Ziegler (52). Vinc −/− MEFs were stably modified with a FRET-based vinculin tension sensor (VinTS) (41) or a vinculin mutant tension sensor that harbors mutations that prevent vinculin-talin (VinTS A50I) or vinculin-actin (VinTS I997A) interactions (30,53) using lentiviral transduction, as previously described (54). All MEFs were maintained in high-glucose Dulbecco's Modified Eagle's Medium (D6429; Sigma-Aldrich, St. Louis, MO) supplemented with 10% fetal bovine serum (HyClone, Logan, UT), nonessential amino acids (Gibco, Waltham, MA), and antibiotic-antimycotic solution (Sigma-Aldrich). HEK293-T cells, used for viral production, were maintained in high-glucose Dulbecco's Modified Eagle's Medium with L-glutamine and sodium bicarbonate (D5796; Sigma-Aldrich) supplemented with 10% fetal bovine serum (HyClone) and antibiotic-antimycotic solution (Sigma-Aldrich).

Generation of viral expression constructs

Construction of pcDNA3.1-VinTS transient expression constructs has been described previously (41). Mutant versions of the VinTS deficient in actin binding (I997A) or talin binding (A50I) were generated via PCR. Specifically, the vinculin tail domain with I997A mutation was generated using forward primer 5′-AGC GGC CGC GGA GTT CCC AGA GCA G-3′, reverse primer 5′-GTC TAG ATT ACT GAT ACC ATG GGG TCT TTC TG-3′, and template DNA pET15b GgVcl 884-1066 ΔAB (generous gift from Dr. Sharon Campbell). The product was inserted into pcDNA3.1-VinTS using 5′-NotI/3′-XbaI, yielding pcDNA3.1-VinTS-I997A. An analogous strategy was used to generate pcDNA3.1-VinTS-A50I using forward primer 5′-AAT AAG CTT GCC ATG CCC GTC TTC CAC AC-3′, reverse primer 5′-GCC GGA TCC GCA AGC CAG TTC-3′, template DNA pEGFPC1/GgVcl 1-851 A50I mutant (Plasmid No. 46269; Addgene, Cambridge, MA), and 5′-HindIII/3′-BamHI restriction sites. To achieve

lentiviral expression of VinTS and mutant VinTS constructs, these constructs plus the upstream CMV-promoter were extracted via 5′*Nru*I/3′*Xba*I digestion and ligated (T4 DNA Ligase; New England BioLabs, Ipswich, MA) into pRRL vector that had been digested with 5′*Eco*RV/3′*Xba*I.

Establishing endogenous vinculin expression

To enable verification of endogenous expression levels of VinTS for each cell analyzed, we used an immunofluorescence-based approach. First, primary antibody species specificity was established by comparing relative immunofluorescent labeling of mouse vinculin-Venus and chicken vinculin-Venus expressed in a vinculin null background with a vinculin antibody (mouse anti-vinculin V9131; Sigma-Aldrich) and a secondary antibody tagged with Alexa-647 (Thermo Fisher Scientific, Waltham, MA). Then, WT MEFs and VinTS-expressing Vinc −/− MEFs were immunofluorescently labeled with the same protocol. Mean intensity for Alexa-647 labeling at FAs in WT MEFs, corrected for antibody specificity, was taken as a standard for endogenous vinculin expression. Mean Venus intensity of VinTS-expressing Vinc −/− MEFs that also showed the Alexa-647 labeling consistent with this endogenous level was used to determine the sensor expression level that corresponds to endogenous vinculin expression. Subsequent analyses were only performed on VinTS-expressing cells within this range.

Cell seeding

Glass-bottom dishes (World Precision Instruments, Sarasota, FL) were incubated with 10 μg/mL fibronectin (FN; Thermo Fisher Scientific) in PBS at 4°C overnight. Dishes were rinsed once with PBS before cell seeding. MEFs were seeded with 25,000 cells per dish and allowed to spread in complete media for 2 h and then in imaging media (Gibco Medium 199 + 10% FBS) for another 2 h.

Inhibition of the actin-myosin cytoskeleton

To inhibit myosin functionality, cells were treated with the ROCK inhibitor Y-27632 (Sigma-Aldrich). MEFs were treated with 25 μM Y-27632, diluted from a 10 mM stock solution in deionized H_2O, 20 min before live imaging. To inhibit actin polymerization, cells were treated with latrunculin A. MEFs were treated with 250 nM latrunculin A (Sigma-Aldrich), diluted from a 2 mM stock solution in DMSO. The cells were allowed to spread for 4 h before inhibitor treatment.

FRET and FRAP imaging

Samples were imaged at 60× magnification (UPlanSApo 60×/NA1.35 Objective; Olympus, Tokyo, Japan) using epifluorescent microscopy on an inverted fluorescent microscope (IX83; Olympus) illuminated by a LambdaLS equipped with a 300 W ozone-free xenon bulb (Sutter Instrument, Novato, CA). The images were captured using a sCMOS ORCA-Flash4.0 V2 camera (Hamamatsu Photonics, Hamamatsu City, Japan). The FRET images were acquired using a custom filter set comprised of an mTFP1 excitation filter (ET450/30×; Chroma Technology, Bellows Falls, VT), mTFP1 emission filter (ET485/20 m; Chroma Technology), Venus excitation filter (ET514/10×; Chroma Technology), Venus emission filter (FF01-571/72; Semrock, Rochester, NY), and dichroic mirror (T450/514rpc; Chroma Technology). User-chosen regions of interest were photobleached using a 515-nm laser (FRAPPA; Andor Technology, Belfast, Northern Ireland) after taking four prebleach images. To ensure complete bleaching, 10 laser pulses with a dwell time of 1000 μs per pixel were used. Pre- and postbleach FRAP images were acquired using the aforementioned Venus excitation and emission filters every 5 s until 5 min postbleach. The motorized filter wheels (Lambda 10-3; Sutter Instrument) and automated stage (H117EIX3; Prior Scientific, Rockland, MA), as well as photobleaching and image acquisition, were controlled through MetaMorph advanced software (Olympus).

FRET efficiency calculations from sensitized emission

FRET was detected through measurement of sensitized emission (55) and quantified using custom-written code in MATLAB (The MathWorks, Natick, MA). A complete description of the FRET efficiency calculations can be found in our previous publications (54,56). Briefly, FRET images were corrected for uneven illumination, coregistered, and background-subtracted. Then, intensity due to spectral bleed-through was removed from the FRET images to obtain corrected FRET images. FRET efficiency was calculated using G and k factors obtained from imaging donor-acceptor fusion constructs of differing, but constant, FRET efficiencies. These constants were also used to calculate the relative concentration of donor and acceptor fluorescent proteins in a sample (55). Cells with average donor-to-acceptor ratios <0.5 or >1.5 were excluded from analysis.

Automated FA segmentation and quantification

Further image analysis was performed using custom-written code in the software MATLAB. For all FRET images, FAs were identified in the acceptor channel, which is proportional to vinculin concentration. The FAs were segmented using the water algorithm, as previously described (57), and each identified adhesion was considered a single unit. For each adhesion, average FRET efficiency, average acceptor intensity, FA area, and donor-to-acceptor ratio values were calculated. The result of the FA segmentation was output as a binary mask, which was then applied across all images resulting from FRET analysis for visualization of data. This mask was inverted to identify FRET efficiency in the cytosol, outside of FAs. To identify single cells on an image, closed boundaries were drawn by the user based on the unmasked acceptor channel image. FAs outside cell boundaries were discarded. Line scans of single FAs, drawn axially starting from the tip of FAs distal to the cell body, were performed using the software ImageJ (National Institutes of Health, Bethesda, MD). Specifically, the Line tool was used to visualize the acceptor channel intensity profile across single, large FAs in the cell periphery. The coordinates of these lines were then transferred to masked FRET efficiency images. Acceptor intensity and FRET efficiency profiles from single FAs were saved as text files for subsequent analysis.

FRAP analysis

Calculation of FRAP recovery was accomplished as previously described (41). Briefly, user-defined polygons were used to outline a background region outside the cells, the initial position of an unbleached FA, and the initial position of a bleached FA. The FA polygons were refined using the water algorithm (57) with user-optimized parameters, and were automatically moved to account for small (2–20 pixels) movements. For bleached FAs, the position of the polygon was held constant until the intensity of the FA reached a user-defined threshold, typically 25% of the initial intensity. FAs that grew, shrank, or moved drastically during the experiment were not analyzed.

The recovery curve was normalized to account for initial intensity, background intensity, and global bleaching. Normalizing for global photobleaching was performed by tracking adhesions that were not specifically photobleached, according to previously established methods (58). The normalized recovery curve was then fit to a single exponential recovery equation:

$$Normalized\ Recovery = R_f - \left(R_f - R_o\right)e^{-kt},$$

where R_f is the final recovery, R_o is the initial recovery, and k is the recovery rate. The half-time of the recovery is determined by $\tau_{1/2} = \ln 2/k$.

Cell protrusion measurement

To measure cell protrusions, Vinc −/− MEFs stably expressing the vinculin tension sensor variants (VinTS, VinTS A50I, and VinTS I997A) were transiently transfected with LifeAct tagged with mCherry using standard Lipofectamine 2000 protocols. Cells were imaged on the Olympus inverted fluorescence microscope in the TRITC channel (excitation filter 560/25 nm, emission filter 607/36 nm; Semrock) every 1 min for 30 min. Individual cells were identified by applying a threshold to the images. The masks were refined using an extended-minima transform and a watershed algorithm to identify the cell boundaries. To calculate area change between time points, masks generated at subsequent time points were subtracted, and the absolute total area change was calculated. For each cell, the average area change per time step was calculated and represents one data point.

Random cell migration

Cells were serum-starved for 2 h before plating onto FN-coated glass-bottom culture dishes in DMEM containing 0.5% BSA. Cells were allowed to attach and spread for 3 h before image acquisition. Time-lapse microscopy was performed on an incubator-housed microscope (20× objective, VivaView FL; Olympus) with a camera (Orca ER/AG type c4742-80-12AG; Hamamatsu Photonics) with image acquisition every 10 min for 10 h. Cell velocity was measured with the software ImageJ using the Manual Tracking plug-in.

Directed cell migration

The bottoms of 8-μm-pore Transwell inserts (Corning, Corning, NY) were coated with 10 μg/mL FN. Cells were serum-starved for 2 h before plating equal numbers of cells into the wells and were given 4 h to migrate before fixation with ice-cold ethanol. Cells from the upper chamber were gently removed with a cotton swab and the migrated cells on the lower chamber were stained with Alexa-488-conjugated phalloidin and Hoechst 33342. To quantify the number of cells that successfully underwent haptotaxis, images taken of the Hoechst-33342-stained nuclei were thresholded to isolate nuclei. The built-in MATLAB function "bwboundaries" was used to assign an ID to each object in the image. Objects below an area of 25 pixels were discarded as too small to be nuclei, and the number of remaining objects were counted as nuclei.

FRET efficiency calculations from spectrofluorimetry

Hypotonic lysates were prepared from HEK293 cells and spectrofluorimetric analyses were performed as previously described (59), with FRET efficiency calculated using the acceptor ratio method (60).

Statistics

Statistical analyses were performed using the software JMP Pro 12 (SAS; https://www.jmp.com/en_dk/software/jmp-12-archive/jmp-pro-12.html). Before combining data sets from independent experiments, statistical tests were performed to ensure no detectable differences between data from the same experimental group. Approximately normal data was analyzed using parametric tests, including ANOVA and Tukey's HSD test. Data sets found to contain unequal variances by Levene's Test were analyzed with nonparametric tests, using the Steel-Dwass multiple comparison test. To compare slopes to zero or against each other, t-tests were performed with Bonferroni corrections to account for multiple comparisons, if relevant. To compare distributions of Venus intensity between cells expressing the different vinculin sensors, a Kolmogorov-Smirnov test was performed between each pair with corrections for multiple comparisons. A p value of $p < 0.05$ was considered statistically significant.

Code availability

All image analysis code is available upon request.

RESULTS

Measuring force-sensitive protein dynamics of vinculin in living cells

Recently, we and others have developed a variety of FRET-based sensors that report the molecular forces experienced by specific proteins in living cells (41,56,61,62). We used a tension-sensitive module (TSMod) composed of two fluorescent proteins capable of undergoing FRET, mTFP1 and Venus A206K, linked by an extensible poly-peptide linker (Fig. 1 A). When incorporated into a protein of interest and subjected to tension, the linker extends, causing a reduction in FRET efficiency (Fig. 1 A). To study the role of vinculin load in living cells, we used the VinTS constructs generated using this method (41).

To enable the probing of force-sensitive protein dynamics of vinculin in living cells, we devised a method that combines FRET-based tension sensors to report the forces experienced by the protein with FRAP to measure protein dynamics; we refer to this combination of techniques as "FRET-FRAP." Specifically, a stably adherent cell expressing VinTS is imaged in three channels (donor excitation/emission, acceptor excitation/emission, and donor excitation/acceptor emission) to obtain the FRET efficiency of the sensor in all FAs (Fig. 1 B). Then, a single FA is photobleached and monitored over time for fluorescence recovery in the acceptor channel, yielding information about the rate and degree of protein turnover (Fig. 1, C and D). When performed sequentially in the same cell, and by gathering data from multiple cells, the correlation between FRET efficiency and half-time of FRAP recovery in single FAs can be used to obtain direct information about the relationship between mechanical load and vinculin dynamics. For example, if vinculin turnover is increased with increased vinculin load, we call this a "force-destabilized" state (Fig. 1 E). Similarly, if the vinculin turnover is decreased with increased vinculin load, we call this a "force-stabilized" state (Fig. 1 F). Here, we discuss the FRET and FRAP results individually before discussing the implications for force-sensitive protein dynamics.

Mechanical loading of vinculin requires the ability to bind actin, but not talin

We sought to determine the key molecular linkages mediating the loading of vinculin in living cells to later assess their roles in force-sensitive protein dynamics. To isolate the effects of vinculin-talin and vinculin-actin interactions in establishing vinculin load in living cells, we incorporated previously characterized vinculin point mutations within VinTS. To perturb talin binding, VinTS A50I was created
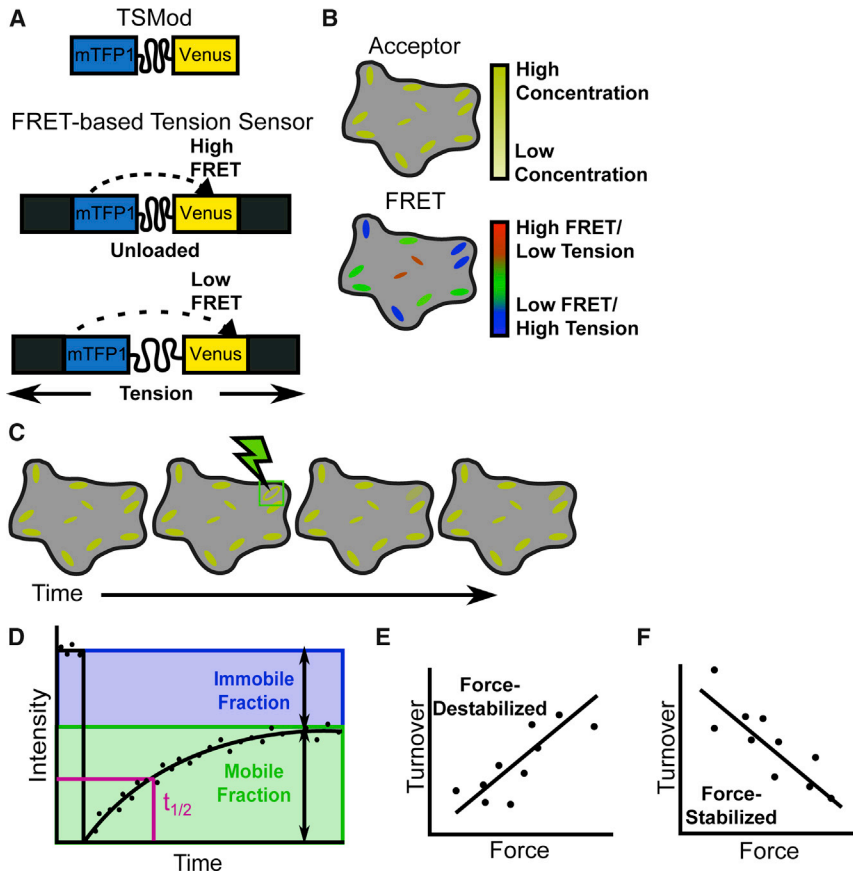
FIGURE 1 Principles of FRET-FRAP technique. (*A*) Schematic is given of the FRET-based TSMod inserted into a protein of interest and the effect of tension on the FRET signal. (*B*) To quantify FRET using sensitized emission, images are taken to capture the donor signal (data not shown), the acceptor signal, and the FRET signal. With appropriate corrections, the FRET image can be assigned a colorimetric scale to visualize how much tension is being applied to the sensor. (*C*) FRAP is conducted using the acceptor signal, which is directly proportional to the concentration. (*D*) FRAP imaging analysis produces curves of fluorescence intensity over time that can be fit using mathematical models to determine protein dynamics. (*E* and *F*) When FRET and FRAP are combined, force and turnover in a single FA can be measured. Measuring multiple FAs in multiple cells yields a relationship between protein load and protein turnover. We refer to a relationship in which increased load correlates with increased turnover as a "force-destabilized" state (*E*). We refer to a relationship in which increased load correlates with increased turnover as a "force-stabilized" state (*F*). To see this figure in color, go online.

(Fig. 2 *A*). Along with disrupting talin binding, this point-mutation results in a 2–3-fold increase in head-tail inhibition in vitro, causing vinculin A50I to be in the closed conformation constitutively (42,53). To perturb actin binding, VinTS I997A was created (Fig. 2 *A*). This point-mutation strongly disrupts vinculin binding to actin, although maintaining the ability of vinculin to bind to PIP$_2$ and undergo conformation regulation (42,63). A lentivirus-based delivery method was used to stably transduce Vinc $-/-$ MEFs with the original VinTS and mutant sensor constructs (54), hereto referred to as "VinTS MEFs," "VinTS A50I MEFs," and "VinTS I997A MEFs." Comparable expression of VinTS, VinTS A50I, and VinTS I997A at FAs was verified by fluorescent imaging of the acceptor channel, which is directly proportional to sensor concentration (Fig. S1).

To verify that the biological effects of these mutations are maintained when incorporated into VinTS, we determined whether the mutated versions of VinTS elicited the alterations in cell size, FA size, and FA distribution within cells demonstrated for vinculin mutants in previous work (30,64). Consistent with previous work with vinculin mutants, the expression of VinTS A50I led to smaller FAs, increased cell spread area, and reduced percentage of the cell area containing FAs, and VinTS I997A led to increased percentage of cell area containing FAs and a slight nonsignificant increase in FA area (Fig. S2). These

data show that, just as WT vinculin function was not perturbed by the incorporation of the TSMod (41), the mutated versions of VinTS have the same biological effects as the mutated forms of vinculin. Additionally, using either spectrofluorimetry- (59,60) or microscopy-based approaches, we verified that all VinTS constructs reported no loads in solution or in the cytosol of cells (Fig. S3). These data demonstrate that the tension sensors function as expected in the absence of load.

To determine the role of vinculin-actin and vinculin-talin interactions on the loads supported by vinculin in living cells, MEFs expressing each of the VinTS constructs were imaged and analyzed to calculate FRET efficiency (Fig. 2, *B* and *C*). We previously established that the unloaded FRET efficiency of the tension sensor module is 28.6% and that lower efficiencies indicate increased tensile loads across vinculin (41,54). FRET efficiencies >28.6% are likely due to statistical fluctuations in the data. The sensor is calibrated in the tensile regime (41), allowing for conversion of FRET efficiency to tensile forces; however, the tension sensors are not calibrated for FRET efficiencies above the unloaded state, thus we cannot report force values for these FRET efficiencies. For this reason, all statistical analyses were performed on quantifications of FRET efficiency. Furthermore, due to incidence of unequal variance between some of the groups, we used nonparametric statistical tests
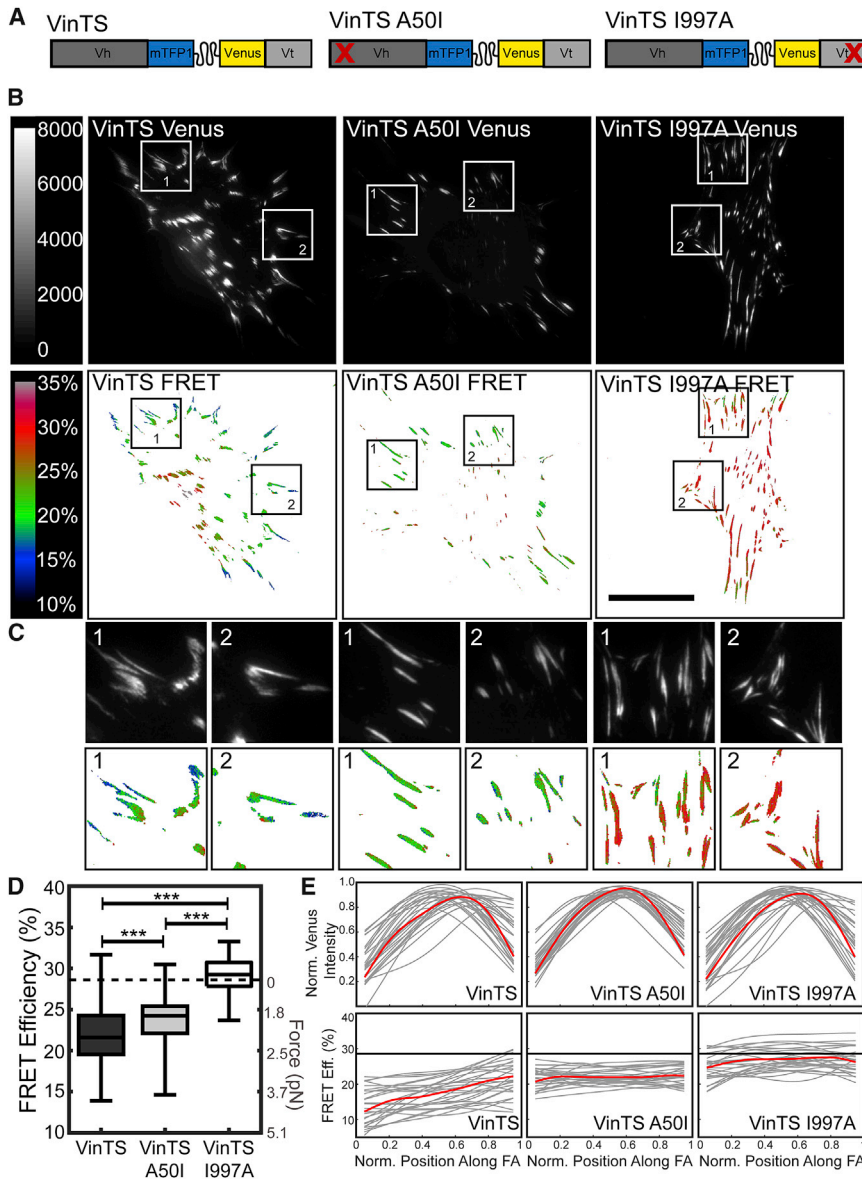
FIGURE 2 Load across vinculin is strongly affected by the ability of vinculin to bind actin, but not talin. (*A*) TSMod was inserted into vinculin variants. (*Left to right*) Shown here is WT VinTS, mutation disrupting the vinculin binding to talin (A50I), and mutation disrupting the vinculin binding to actin (I997A). (*B*) Representative acceptor (*top row*) and masked FRET efficiency (*bottom row*) images are given of single Vinc −/− MEFs expressing each of the VinTS constructs. Scale bars, 30 μm. (*C*) Zoomed-in view is given of the regions indicated in (*B*). (*D*) A box-whisker plot is given of cell-averaged FRET efficiency (n = 150, 166, and 79 cells, respectively, from seven independent experiments) compared to previously established zero-load (*dotted line*). Differences between groups were detected using the Steel-Dwass test (***$p < 0.001$); p values for all comparisons can be found in Table S1. (*E*) Line scans are shown of vinculin distribution and FRET efficiency across peripheral FAs from distal to proximal tip. Thin lines represent each individual adhesion (n = 27 FAs from three independent experiments); thick lines represent a smoothing spline fit to the collective FA data. To see this figure in color, go online.

in the evaluation of this data (see Materials and Methods for details, and Table S1).

Consistent with our previous work, we found that VinTS reported a FRET efficiency of 21.8% (Fig. 2 *D*), corresponding to tensile loading (2.0 pN). Interestingly, FRET efficiencies reported by VinTS A50I, which has deficient talin-binding, showed that VinTS A50I is still under substantial load, although statistically significantly less load than VinTS (23.6%, 1.6 pN; Fig. 2 *D*). By contrast, VinTS I997A, which has deficient actin-binding, exhibited a cell-average FRET efficiency of 29.3%, statistically distinct from both VinTS and VinTS A50I and indistinguishable from the unloaded state of the sensor (Fig. 2 *D*). Further demonstration of the difference in mechanical loading experienced by VinTS and VinTS A50I can be seen by evaluating the distribution of vinculin tension within individual FAs. As

shown in Fig. 2 *C*, there is significant spatial variation in the load reported by VinTS at single FAs that is not apparent in the other constructs. We quantified the spatial variation in loads reported by these sensors within individual peripheral FAs using line scans. Although the spatial distribution of vinculin is similar across the different mutants, the loads experienced by VinTS within a single FA spatially vary with highest loads at the distal tips of FAs, in agreement with previous work (65). Notably, there are no spatial variations reported by VinTS A50I or VinTS I997A (Fig. 2 *E*). In summary, these results demonstrate that the ability of vinculin to interact with actin is required for mechanical loading within FAs, whereas interactions between vinculin and talin are not. The observed difference in the spatial dependence of VinTS and VinTS A50I indicate these constructs are not in identical mechanical states despite both being under load.

Vinculin dynamics within focal adhesions are affected by an inability to bind talin

To probe the effects of altered vinculin-talin and vinculin-actin interactions on the dynamics of vinculin at FAs, we subjected Vinc $-/-$ MEFs expressing the various VinTS constructs to FRAP analysis. Previous work has shown the insertion of the tension sensor module into vinculin does not affect vinculin dynamics (41), and we ensured that FRET imaging before FRAP acquisition does not affect measurements of vinculin dynamics (Fig. S4). A difference in recovery among the various VinTS constructs was evident when looking at a representative FA from cells expressing one of the VinTS constructs (Fig. 3 A; Videos S1, S2, and S3). By 60 s postbleach, VinTS A50I was already beginning to recover, whereas both VinTS and VinTS I997A showed no visually detectable recovery, which was also apparent in the FRAP curves (Fig. 3 B).

To quantify vinculin dynamics, we fit the FRAP data to a standard exponential recovery curve defined by two parameters: a half-time of recovery and an immobile fraction. Statistically significant differences in the variance of groups was observed, requiring the use of nonparametric statistical tests (Table S2). The half-time of recovery of VinTS (163.7 s) is statistically different from VinTS A50I (94.48 s), but not VinTS I997A (143.9 s) (Fig. 3 C). The average mobile fraction of VinTS A50I (68.8%) is significantly higher than the VinTS (40.9%) or VinTS I997A (28.5%) (Fig. 3 D). Notably, there is no discernable statistical difference between the dynamics of VinTS or VinTS I997A in this analysis. We note that these measurements of vinculin dynamics differ from those reported previously in the literature (41,51,53,66), exhibiting longer

recovery times and higher immobile fractions. These differences are not due to the inclusion of TSMod (Fig. S4) or nonphysiological expression levels. Vinculin turnover has been shown to be regulated by cytoskeletal contractility (40,47,48), phosphorylation state (67), and substrate stiffness (68), suggesting that vinculin half-time and mobile fraction are not characteristic values, but depend strongly on context.

Overall, these results indicate that vinculin-talin interactions are critically important for stabilizing vinculin at FAs, which is consistent with previous work (53,67). Surprisingly, disturbing vinculin-actin interactions did not lead to detectable changes in vinculin dynamics. However, based on measurements of the mechanical loading, we expect a significant percentage of FAs have vinculin that is not appreciably loaded. An inability to isolate this population could confound detection of force-dependent effects.

Vinculin is loaded by distinct mechanisms depending on vinculin-talin interactions

To investigate the role of cytoskeletal contractility on vinculin load, Vinc $-/-$ MEFs expressing the VinTS constructs (Fig. 4 A) were treated with 25 μM of the ROCK inhibitor Y-27632 for 20 min, as described in previous work (48). This treatment duration was the shortest capable of resulting in statistically significant loss of loading across vinculin. This treatment resulted in significant changes in cell and FA morphologies for all cell lines (Fig. 4, B and C). Also, the FRET signals reported by VinTS constructs localized to the cytosol did not change, indicating the inhibitor did not affect the function of the sensors (Fig. S5).
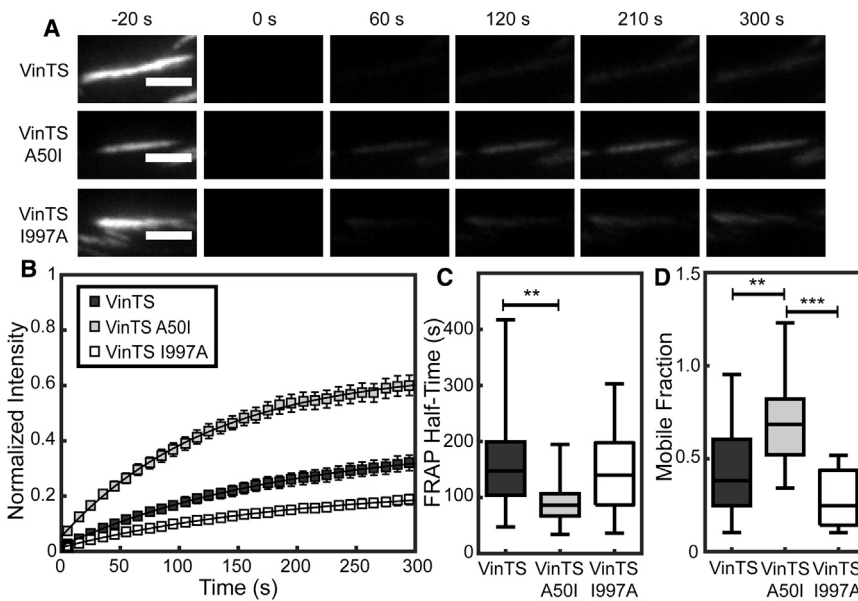

FIGURE 3 Vinculin dynamics are strongly affected by the ability of vinculin to bind talin, but not actin. (A) Representative FAs of cells expressing the VinTS and its mutant variants (VinTS A50I, VinTS I997A) are displayed in the acceptor channel during FRAP imaging. Scale bars, 3 μm. (B) Vinculin FRAP recovery curves are shown for cells expressing VinTS, VinTS A50I, or VinTS I997A ($n = 34$, 21, and 18 FAs, respectively, from seven independent experiments). (C) Box-whisker plots are given of the half-time of recovery for the FAs that were analyzed in (B). (D) Box-whisker plots are given of the mobile fraction for the FAs that were analyzed in (B). Differences between groups were detected using the Steel-Dwass test (**$p < 0.01$, ***$p < 0.001$); p values for all comparisons can be found in Table S2.
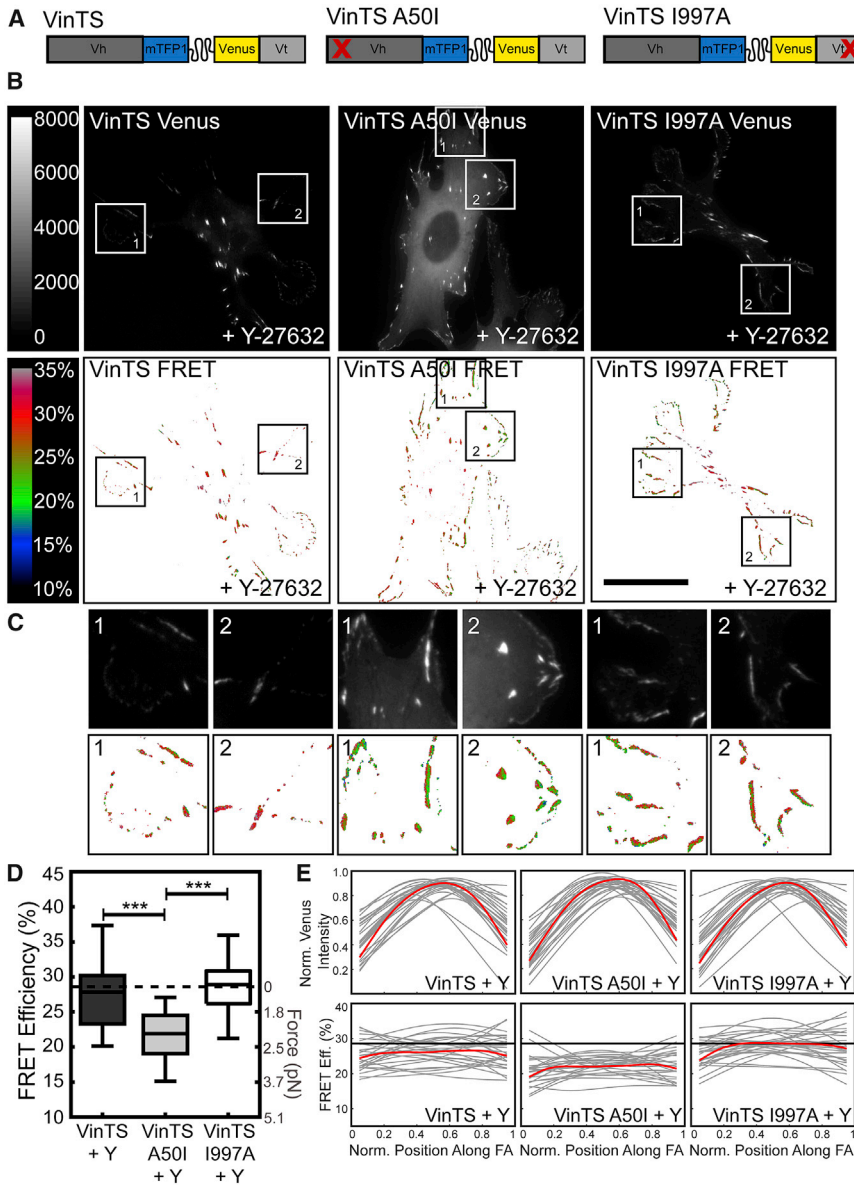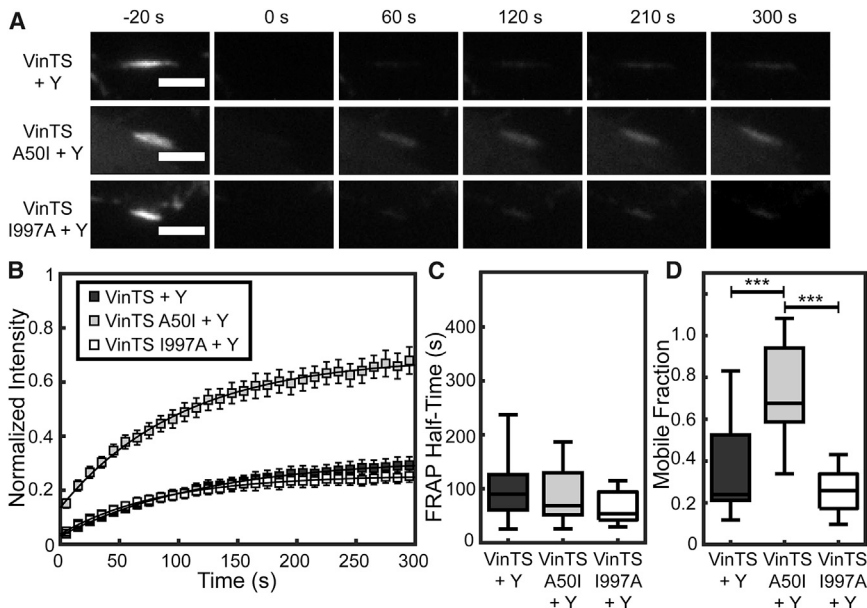
FIGURE 4 Reduction of cytoskeletal tension via ROCK inhibition affects vinculin load only in the presence of vinculin-talin interaction. (*A*) VinTS variants are shown. (*B*) Representative acceptor (*top row*) and masked FRET efficiency (*bottom row*) images are given of single Vinc −/− MEFs expressing each of the VinTS constructs; these constructs were treated with 25 μM Y-27632. Scale bars, 30 μm. (*C*) Zoomed-in view is given of the regions indicated in (*B*). (*D*) A box-whisker plot is given of cell-averaged FRET efficiency ($n = 34$, 60, and 53 cells, respectively, from four independent experiments) compared to previously established zero-load (*dotted line*). Differences between groups were detected using the Steel-Dwass test (***$p < 0.001$); p values for all comparisons can be found in Table S1. (*E*) Line scans are shown of vinculin distribution and FRET efficiency across peripheral FAs from distal to proximal tip. Thin lines represent each individual adhesion ($n = 27$ FAs from three independent experiments); thick lines represent a smoothing spline fit to the collective FA data. To see this figure in color, go online.

ROCK inhibition decreased VinTS load in FAs to a level consistent with the zero-force state, exhibiting a cell-average FRET efficiency of 27.7% (0.58 pN; Fig. 4 *D*; Table S1), agreeing with previous work (41). Additionally, there was significantly less spatial variation of the mechanical loads reported by VinTS within FAs when cells were exposed to Y-27632 (Fig. 4 *E*). ROCK inhibition had no discernable effect on the average FRET reported by VinTS I997A (29.3 vs. 28.8%; Fig. 4 *D*), which is consistent with a lack of mechanical loading. This result is not surprising, given inability of this construct to bind actin. Interestingly, ROCK inhibition resulted in a slight increase in load reported by VinTS A50I (23.6 vs. 21.7%, 1.6 vs. 2.1 pN; Fig. 4 *D*). The differential response of VinTS and VinTS A50I to ROCK inhibition suggests that distinct mechanisms are loading these constructs.

To further investigate the molecular processes mediating the mechanical loading of VinTS A50I, we generated a VinTS construct with both the A50I and I997A mutations. This construct localizes to FAs but does not bear significant forces (Fig. S6). This indicates that VinTS A50I is being loaded through binding to actin. Next, we used a low dose of latrunculin A to inhibit actin polymerization while maintaining stress fibers. We found that VinTS load is unaffected by this treatment, but VinTS A50I has significantly reduced load (Fig. S7). In total, these data show that both VinTS and VinTS A50I require actin binding to be loaded but involve distinct mechanisms. VinTS is loaded by a ROCK-dependent but dynamic actin-independent mechanism, likely myosin activity within stress fibers, whereas VinTS A50I is loaded in an actin polymerization-dependent manner.

FIGURE 5 Reduction of cytoskeletal tension via ROCK inhibition affects vinculin dynamics only in the presence of vinculin-talin interaction. (A) Representative FAs of cells expressing the VinTS and its mutant variants (VinTS A50I, VinTS I997A) treated with 25 μM Y-27632 are displayed in the acceptor channel during FRAP imaging. Scale bars, 3 μm. (B) Vinculin FRAP recovery curves are shown for cells expressing VinTS, VinTS A50I, or VinTS I997A (n = 24, 16, and 16 FAs, respectively, from four independent experiments). (C) Box-whisker plots are given of the half-time of recovery for the FAs analyzed in (B). No significant difference was detected between groups. (D) Box-whisker plots of the mobile fraction are given for the FAs analyzed in (B). Differences between groups were detected using the Steel-Dwass test (***$p < 0.001$); p values for all comparisons can be found in Table S2.

Reduction of actomyosin contractility through ROCK inhibition requires vinculin-talin interaction to affect vinculin dynamics

To study the role of the ROCK-dependent force generation by the actomyosin network in vinculin dynamics, following previous work (48), we treated Vinc $-/-$ MEFs expressing the VinTS constructs with 25 μM of the ROCK inhibitor Y-27632 for 20 min directly before FRAP imaging. Other work has demonstrated that longer incubation times with Y-27632 lead to a major decrease in the amount of vinculin at FAs and reduction of vinculin mobile fraction (47). We have verified these same results in our system. As these long-term effects could be due to secondary responses involving bulk disassembly of the actomyosin network or changes in the composition of the FAs instead of an immediate loss of mechanical loading, we choose to focus on the earlier time points in this work.

ROCK inhibition of cells expressing the different mutants resulted in all groups having similar rates of vinculin recovery in FAs but did not cause changes in mobile fraction (Fig. 5, A and B; Table S2). ROCK inhibition resulted in a statistically significant faster average half-time of recovery in both VinTS MEFs (101.6 s, Fig. 5, B and C; Table S2; and Video S4) and VinTS I997A MEFs (66.72 s; Fig. 5, B and C; Video S6). VinTS A50I MEFs exhibit no statistically significant changes in response to ROCK inhibition (Fig. 5, B–D; Video S5), indicating that the effect of ROCK inhibition on vinculin dynamics requires vinculin-talin interactions. VinTS A50I is still loaded in response to ROCK inhibition, whereas the VinTS and VinTS I997A are not, even though all exhibit rapid turnover under ROCK inhibition. Thus, a simple lack of mechanical loading of all constructs cannot account for the similarity of the dynamics

of these sensors. This suggests that the reduction in cytoskeletal tension due to ROCK inhibition is responsible for regulating the vinculin dynamics of VinTS and VinTS I997A, whereas VinTS A50I dynamics remain ROCK-independent.

Vinculin exhibits context-dependent force-sensitive dynamics

Inhibition of vinculin-actin interactions and vinculin-talin interactions had drastically different effects on vinculin loading and vinculin dynamics; thus, we used a unique combination of FRET and FRAP to investigate the force-sensitive protein dynamics of vinculin and examine the effects of vinculin-talin or vinculin-actin interactions on this relationship. In VinTS MEFs, increased vinculin tension was associated with longer vinculin half-times of recovery (Fig. 6 A), corresponding to the force-stabilized state of vinculin at the FA. In contrast, in VinTS A50I MEFs, increased vinculin tension was associated with shorter vinculin half-times of recovery (Fig. 6 B), consistent with the force-destabilized state. In VinTS I997A cells, we observe no relationship between vinculin tension and the half-time of recovery (Fig. 6 C).

The use of the ROCK inhibitor Y-27632 on VinTS MEFs resulted in reversal of the vinculin force-dynamics relationship with respect to untreated VinTS MEFs to the force-destabilized state (Fig. 6 D). In VinTS A50I MEFs, ROCK inhibition had no discernable effect on vinculin force-sensitive dynamics, maintaining the same force-destabilized state (Fig. 6 E). Finally, in VinTS I997A MEFs treated with ROCK inhibitor, vinculin dynamics were still insensitive to force (Fig. 6 F), although a reduction
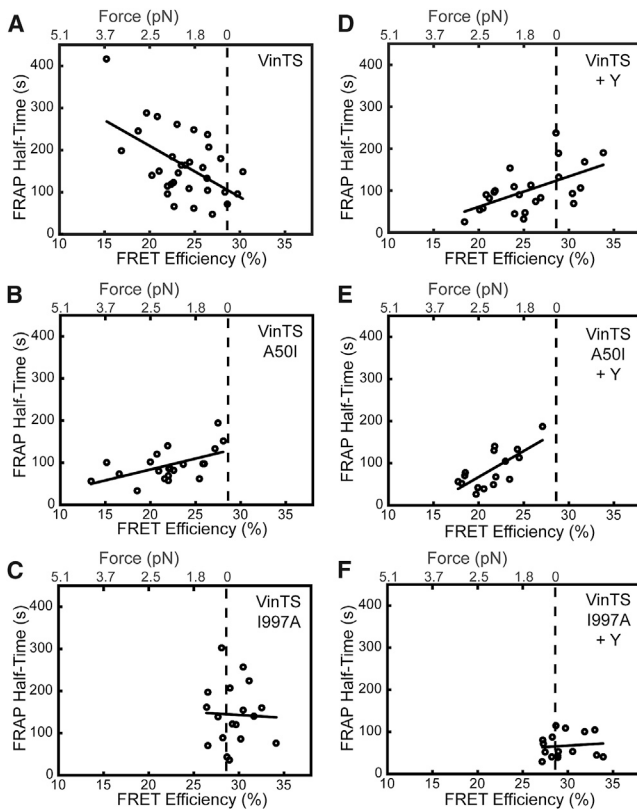
FIGURE 6 FRET-FRAP assay shows that force-sensitive vinculin dynamics depend on talin and actin interactions. (*A*) Correlation between recovery half-time and FRET efficiency for WT vinculin corresponds to the force-stabilized state ($n = 32$, $p < 0.005$). (*B*) Correlation between recovery half-time and FRET efficiency for VinTS A50I corresponds to the force-destabilized state ($n = 21$, $p < 0.05$). (*C*) No detectable correlation between recovery half-time and FRET efficiency was observed for VinTS I997A ($n = 18$, $p = 0.88$). (*D*) Y-27632 treatment reverses the relationship between recovery half-time and load for WT vinculin, corresponding to the force-destabilized state ($n = 24$, $p < 0.05$). (*E*) Y-27632 treatment does not affect the relationship between recovery and load for VinTS A50I, which remains in the force-destabilized state ($n = 16$, $p < 0.01$). (*F*) Y-27632 treatment does not affect the relationship between recovery and load for VinTS I997A, with turnover still insensitive to load ($n = 16$, $p = 0.98$). The *p* values indicate the results of a *t*-test comparing the regression slope to zero. (*Vertical dotted lines*) Previously established zero-load is shown.

in the overall recovery time was observed. Quantification of the FRET-FRAP regression slopes can be seen in Fig. S8. We also evaluated the effects of load on the vinculin mobile fraction for the cells expressing each tension sensor construct but found that mobile fraction is entirely insensitive to load in all conditions (Figs. S9 and S10). Additionally, there is no apparent correlation between vinculin half-time and the local amount of VinTS, as determined by the intensity in the Venus channel (Fig. S11).

In summary, these data show that vinculin, depending on the specific protein-protein interactions it can form, exhibits drastically different force-sensitive protein dynamics. Furthermore, vinculin-talin binding, vinculin-actin binding, and ROCK activity are required for the force-based stabili-

zation of vinculin. Also, analysis of the mobile fraction reveals that molecular load only governs the turnover rate of vinculin, not the amount of vinculin that is turning over. As the mobile fraction was also not affected by short-term ROCK inhibition, this data suggests that another process, likely biochemical regulation, determines the percentage of immobile vinculin.
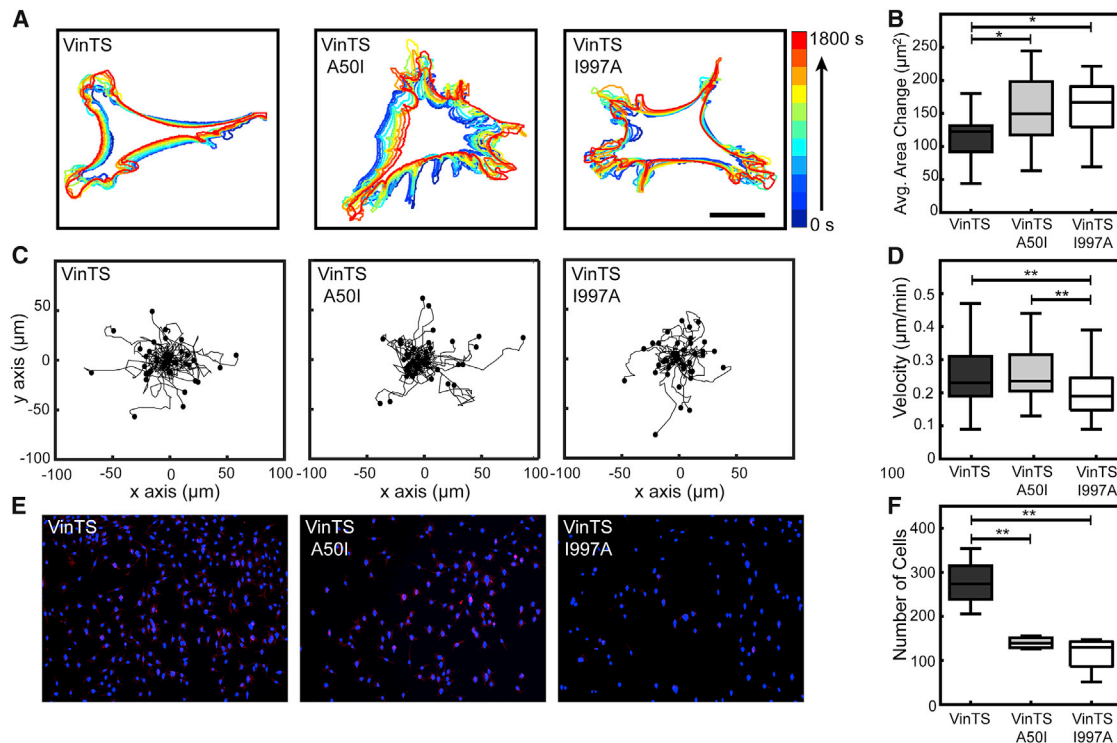
Cell protrusion depends on force-sensitive vinculin dynamics

Next, we sought to elucidate the role of vinculin force-sensitive protein dynamics on other subcellular processes, particularly those important in cell migration. To monitor cell protrusion, Vinc −/− MEFs stably expressing VinTS, VinTS A50I, or VinTS I997A were transiently transfected with mCherry-LifeAct (69), and the spread area of each cell was tracked every 1 min over a period of 30 min. Comparing the cell edges over time revealed that VinTS MEFs generally had stable directional protrusions, whereas VinTS A50I MEFs had protrusive activity without clear direction, and VinTS I997A MEFs had high protrusive activity without movement (Fig. 7 *A*). The total area change between each time step was quantified and averaged for each cell, with VinTS MEFs having the least amount of area change (Fig. 7 *B*). Overall, these data are consistent with the idea that an alteration of the force-sensitive dynamics of vinculin affects protrusion dynamics. Specifically, the force-stabilized state of vinculin seems to be required for the formation of stable directional protrusions.

Directed cell migration is enhanced if vinculin is in the force-stabilized state

Finally, we sought to probe the role of vinculin force-sensitive dynamics in cell migration. To study random cell migration, Vinc −/− MEFs expressing the different VinTS variants were allowed to migrate on FN-coated glass for 10 h. VinTS MEFs were found to migrate at 0.25 μm/s. Comparing across the different VinTS mutants revealed that disruption of talin binding did not significantly alter cell migration speed, whereas disruption of actin binding significantly reduced migration speed (Fig. 7, *C* and *D*). These data demonstrate that, although some form of mechanical coupling with vinculin dynamics is required, both forms of force-sensitive dynamics can mediate random cell migration.

Based on reports demonstrating vinculin's role in three-dimensional migration (3D) (52,70,71), we sought to probe the ability of cells expressing the various VinTS constructs to perform directed migration through confined spaces. We used a Boyden chamber assay as a measure of effective 3D haptotaxis, or migration along a gradient of substrate-bound cues, in this case a fibronectin coating. Equal numbers of cells were seeded in the upper chamber, and after allowing

FIGURE 7 Cell protrusion and migration are affected by vinculin force-sensitive dynamics. (*A*) Representative cell outlines were generated every 3 min for 30 min on Vinc −/− MEFs stably expressing VinTS variants and transiently expressing mCherry-LifeAct. Scale bars, 10 μm. (*B*) The box-whisker plot indicates average area change per 1-min time step for each cell line (*n* =16, 16, and 16 cells, respectively, from three independent experiments). (*C*) Sample trajectories are given of cells expressing VinTS constructs migrating in two dimensions. (*D*) Box-whisker plots are given of random cell migration speed in two dimensions (*n* = 101, 48, and 45 cells, respectively, from three independent experiments). (*E*) Representative fields of view are shown of migrated cells from a Boyden chamber haptotaxis assay. Hoechst 33342 staining (*blue*) identifies the nucleus; phalloidin staining (*red*) identifies the cytoskeleton. (*F*) Box-whisker plots are shown of a number of cells per field of view in a Boyden chamber haptotaxis migration assay (*n* = 4 per group from three independent experiments). Differences between groups were detected using Tukey's HSD test (*$p < 0.05$, **$p < 0.01$). To see this figure in color, go online.

the cells to respond to the FN haptotactic cue for 4 h, the number of cells that crossed through the insert in a single field of view was quantified (Fig. 7 *E*). In this system, the VinTS MEFs displayed the most efficient directed migration, with an average of 277 cells per field of view. Both the VinTS A50I and VinTS I997A MEFs exhibited impaired responses, with averages of only 140 and 115 cells per field of view, respectively (Fig. 7 *F*). These results indicate that the vinculin force-stabilized state is particularly important in coordinating effective directed migration through small pores where cell force generation is likely quite high.

DISCUSSION

In this work, we have combined two established techniques in a novel fashion, to the best of our knowledge, enabling the molecularly specific measurement of force-sensitive protein dynamics in living cells. This technique, which we term "FRET-FRAP," is distinct from previous studies of force-sensitive protein dynamics because the molecular tension sensors enable direct observation of the mechanical loading of a specific protein. By measuring protein load and protein dynamics on the same molecular-scale, FRET-FRAP avoids

potential confounding effects in other methods of cellular force measurements, such as difficulties associated with inferring molecular-specific information from whole-cell mechanical measurements like traction force microscopy, as well as unintended consequences of global perturbation of cell contractility, as might occur when using actomyosin inhibitors. To begin to elucidate the key molecular mediators of the diverse mechanosensitive behaviors of FAs, we applied the FRET-FRAP technique to the mechanical linker protein vinculin. Surprisingly, the nature of the relationship between vinculin load and vinculin dynamics is mutable. Using specific point mutations to selectively inhibit distinct aspects of vinculin function and measuring changes in molecular load in response to actomyosin inhibitors, we observe three mechanically distinct states: the immobile state, the force-stabilized state, and the force-destabilized state.

The immobile state is indicative of the population of vinculin that does not display dynamic turnover. Largely consistent with previous work (67), the comparison of the mobile fractions observed in VinTS and VinTS A50I MEFs shows that vinculin must be able to become active and bind talin to form the immobile state. Interestingly,

we find the mobile fraction of vinculin was not perturbed by impaired vinculin-actin binding or in response to the reduction of actomyosin contractility using ROCK inhibition for short times. Furthermore, unlike the turnover rate of vinculin, the mobile fraction was not correlated with loads experienced by vinculin. Together, these data suggest the mechanical loading of vinculin is not required for the formation or maintenance of the immobile state. It also raises the possibility that the immobile state is not subject to mechanical loading, although this will require further investigation to definitively demonstrate. Notably, previous work using ROCK inhibition with longer incubations of 2 h, did see an alteration in the vinculin immobile fraction (47). These treatment times are significantly longer than the timescales associated with loss of vinculin load, and often result in the bulk disassembly of the actomyosin cytoskeleton. Based on these observations, we suggest that the primary function of the immobile state is to mediate protein scaffolding or signaling events, potentially associated with a stable actomyosin network.

The force-stabilized state describes a population of vinculin whose turnover dynamics are inhibited by the application of mechanical loading. This state is only observed in VinTS MEFs, demonstrating that vinculin-talin and vinculin-actin interactions as well as ROCK-dependent actomyosin structures and processes, such as talin loading, are required. We suggest this state is mediated by active, loaded vinculin interacting with a force-exposed binding site in talin (Fig. S12). Because the FRAP dynamics observed in VinTS MEFs and VinTS I997A MEFs are quite similar, we conclude that the vinculin-talin interaction plays a major role in determining vinculin dynamics, which is consistent with biochemical studies demonstrating the exceptional strength of this interaction (28,29,53). However, load exerted on VinTS results in even slower dynamics, indicating that the ability of vinculin to support load from actin-based structures is critical to the stabilization of this complex. Two likely mechanistic explanations include the formation of vinculin load-dependent stabilizing protein-protein interactions, as has been proposed to occur between vinculin and vinexin (68), and the existence of a catch bond at the vinculin-actin interface (72). Regardless of the exact mechanism, we propose that this two-part stabilization scheme, involving force-sensitive interactions within both the head and tail domains of vinculin, is a key characteristic of the force-stabilized state.

The force-destabilized state describes a population of vinculin whose turnover dynamics are augmented by the application of mechanical loading. This state is observed in VinTS A50I MEFs and VinTS MEFs treated with the ROCK inhibitor. As VinTS A50I I997A does not support loading, actin binding is necessary to provide load on the force-destabilized state. Based on the inability of ROCK inhibition to reduce loads on VinTS A50I load but also the loss of VinTS A50I load with the application of a low

dose of latrunculin A, we suggest actin polymerization as a likely candidate for loading vinculin in this state (Fig. S12). Furthermore, a possible explanation for the slight increase in VinTS A50I tension when treated with the ROCK inhibitor could be an upregulation of the actin polymerization-dependent loading mechanism, although this will have to be evaluated in future work. It has been shown that depending on actin concentration and organization, actin polymerization can generate between 1 and 9 pN of force (73), suggesting that the apparent load on VinTS A50I of ∼2 pN could be generated by actin polymerization. It has been shown that vinculin A50I resides in the closed conformation within FAs (42). Although vinculin in the closed conformation is unable to bind actin in solution (59), it is likely that binding interactions at the FA may induce a shift in vinculin structure without separating the head and tail domain, allowing for actin binding, as suggested in simulations (74,75).

The vinculin A50I mutation drastically reduces the affinity of vinculin for talin in vitro (53), and results in vinculin localization to a lower z plane at the FA (42), suggesting that this force-destabilized state is not mediated by the typical force-sensitive vinculin binding sites on talin (Fig. S12). This is corroborated by the fact that ROCK inhibition, which reduces load on talin (36) and likely obscures these same binding sites, results in the conversion of VinTS from a force-stabilized to a force-destabilized state. However, it is currently unclear what vinculin is binding in its N-terminus to localize to FAs and bear load in this state. Previous work has shown that vinculin and vinculin A50I can interact with phosphorylated paxillin in the C terminus (42), implicating this as a potential mode of recruitment to FAs. Recent work has shown that α-actinin can bind to integrins (76) and that vinculin can bind α-actinin in a force-dependent manner (77), suggesting that α-actinin is a potential binding partner for vinculin A50I or vinculin in a low ROCK-mediated contractility state. Overall, these observations demonstrate that vinculin can adopt a variety of mechanical states, each of which exhibit distinct force-sensitive dynamics within FAs.

To demonstrate the functional importance of these distinct mechanical states of vinculin, we probed their effects on cell protrusion and migration. Both VinTS and VinTS I997A have a similar portion of vinculin in the immobile state, but only VinTS can form the force-stabilized state. Thus, their comparison elucidates the role of the force-stabilized state (Fig. S12). Comparisons involving VinTS A50I MEFs are more complicated, as most of the vinculin is in the force-destabilized state with very little immobile vinculin (Fig. S12). Although persistent protrusion was only observed in the force-stabilized state, VinTS MEFs and VinTS A50I MEFs exhibited equivalent random migration speeds that were significantly faster than VinTS I997A cells. This result demonstrates that both forms of force-sensitive dynamics can equivalently

enable migration. However, only the force-stabilized state could support 3D-directed migration in response to a haptotactic gradient. Overall, these data show that the nature of the force-sensitive dynamics of vinculin is critically important in enabling the coordination of mechanically sensitive subcellular processes to ensure efficient directed migration.

These results also inform efforts to describe the physical mechanisms that enable force transmission through cells. As we demonstrated that vinculin can form multiple connections that bear load, we suggest that there are multiple modes of force transmission via vinculin, or multiple classes of molecular clutches. The force-stabilized state of vinculin appears to rely on both force-induced conformation changes of talin as well as mechanical regulation of vinculin. Vinculin can exhibit force-activated bond dynamics [72] as well as form force-induced protein-protein interactions [68], suggesting a variety of pertinent mechanisms. Although the role of vinculin requires further elucidation, this physical picture is broadly consistent with the latest models of multiprotein molecular clutches in mechanosensing [25,26]. The necessity of this state for coordinating directed cell migration suggests that vinculin force-stabilization is a mechanism for FAs to reinforce force transmission in highly contractile environments, including stiff substrates and confined spaces. As vinculin A50I is closed at FAs and was not unloaded by ROCK inhibition, which would likely unload neighboring proteins, the force-destabilized state of vinculin appears to be regulated solely by mechanical effects on bond dynamics, a state well described by some of the first molecular-clutch models [20,21]. The force-destabilized state dominates under low actomyosin contractility. This suggests that this state is critical in scenarios where fast FA dynamics are observed, including interactions with soft substrates and releasing of adhesions to allow translocation of the cell body during migration. Reports of reduced traction force and adhesion strength in cells expressing vinculin A50I [40,64] are consistent with the idea that the vinculin force-destabilized state reduces force transmission from the cytoskeleton to the ECM, likely due to rapid turnover of vinculin in response to load and interaction with dynamic polymerizing actin rather than stable stress fibers. Together, these data demonstrate that ability of vinculin to adopt distinct mechanical states enables the complex mechanosensitivity of FAs, augmenting force transmission or rearrangement dynamics depending on the vinculin state.

In summary, we have developed a technique for probing force-sensitive protein dynamics and used it to reveal that vinculin can exist in a variety of states that serve as different types of molecular clutches (Fig. S12). Force-sensitive bond dynamics are often probed through in vitro single-molecule biophysics techniques using purified proteins or protein fragments [72,78]. Although these in vitro experiments are uniquely interpretable due to application of a specified force and an isolated environment, FRET-FRAP enables concep-

tually similar measurements in living cells where proteins are subject to regulation. We propose that the combination of these approaches will be particularly powerful in elucidating the molecular-scale regulation and role of force-sensitive proteins dynamics in a variety of subcellular structures, extracellular environments, and cell processes.

SUPPORTING MATERIAL

Twelve figures, two tables, and six videos are available at http://www.biophysj.org/biophysj/supplemental/S0006-3495(18)30250-9.

AUTHOR CONTRIBUTIONS

K.E.R. and B.D.H. were responsible for conceptualization. K.E.R., D.W.S., N.C., and B.D.H. designed the methodology. K.E.R. and B.D.H. carried out the formal analysis. K.E.R., D.W.S., and B.D.H. performed the investigation. D.W.S. and N.C. obtained the experimental resources. K.E.R. and B.D.H. wrote the original draft. K.E.R., D.W.S., N.C., and B.D.H. reviewed and edited the manuscript. B.D.H. was responsible for supervision and acquired the funding.

ACKNOWLEDGMENTS

REFERENCES

1. Lauffenburger, D. A., and A. F. Horwitz. 1996. Cell migration: a physically integrated molecular process. Cell. 84:359–369.

2. Petrie, R. J., A. D. Doyle, and K. M. Yamada. 2009. Random versus directionally persistent cell migration. Nat. Rev. Mol. Cell Biol. 10:538–549.

3. Friedl, P. 2004. Prespecification and plasticity: shifting mechanisms of cell migration. Curr. Opin. Cell Biol. 16:14–23.

4. Keller, R. 2005. Cell migration during gastrulation. Curr. Opin. Cell Biol. 17:533–541.

5. Rose, D. M., R. Alon, and M. H. Ginsberg. 2007. Integrin modulation and signaling in leukocyte adhesion and migration. Immunol. Rev. 218:126–134.

6. Yamaguchi, H., J. Wyckoff, and J. Condeelis. 2005. Cell migration in tumors. Curr. Opin. Cell Biol. 17:559–564.

7. Pollard, T. D., and G. G. Borisy. 2003. Cellular motility driven by assembly and disassembly of actin filaments. Cell. 112:453–465.

8. Geiger, B., J. P. Spatz, and A. D. Bershadsky. 2009. Environmental sensing through focal adhesions. Nat. Rev. Mol. Cell Biol. 10:21–33.

9. Burridge, K., and E. S. Wittchen. 2013. The tension mounts: stress fibers as force-generating mechanotransducers. J. Cell Biol. 200:9–19.

10. Oakes, P. W., and M. L. Gardel. 2014. Stressing the limits of focal adhesion mechanosensitivity. Curr. Opin. Cell Biol. 30:68–73.

11. Parsons, J. T., A. R. Horwitz, and M. A. Schwartz. 2010. Cell adhesion: integrating cytoskeletal dynamics and cellular tension. *Nat. Rev. Mol. Cell Biol.* 11:633–643.

12. Lin, C. H., and P. Forscher. 1995. Growth cone advance is inversely proportional to retrograde F-actin flow. *Neuron.* 14:763–771.

13. Mitchison, T., and M. Kirschner. 1988. Cytoskeletal dynamics and nerve growth. *Neuron.* 1:761–772.

14. Hu, K., L. Ji, …, C. M. Waterman-Storer. 2007. Differential transmission of actin motion within focal adhesions. *Science.* 315:111–115.

15. Case, L. B., and C. M. Waterman. 2015. Integration of actin dynamics and cell adhesion by a three-dimensional, mechanosensitive molecular clutch. *Nat. Cell Biol.* 17:955–963.

16. Chrzanowska-Wodnicka, M., and K. Burridge. 1996. Rho-stimulated contractility drives the formation of stress fibers and focal adhesions. *J. Cell Biol.* 133:1403–1415.

17. Choquet, D., D. P. Felsenfeld, and M. P. Sheetz. 1997. Extracellular matrix rigidity causes strengthening of integrin-cytoskeleton linkages. *Cell.* 88:39–48.

18. Riveline, D., E. Zamir, …, A. D. Bershadsky. 2001. Focal contacts as mechanosensors: externally applied local mechanical force induces growth of focal contacts by an mDia1-dependent and ROCK-independent mechanism. *J. Cell Biol.* 153:1175–1186.

19. Boettiger, D. 2012. Mechanical control of integrin-mediated adhesion and signaling. *Curr. Opin. Cell Biol.* 24:592–599.

20. Chan, C. E., and D. J. Odde. 2008. Traction dynamics of filopodia on compliant substrates. *Science.* 322:1687–1691.

21. Evans, E. A., and D. A. Calderwood. 2007. Forces and bond dynamics in cell adhesion. *Science.* 316:1148–1153.

22. Nicolas, A., B. Geiger, and S. A. Safran. 2004. Cell mechanosensitivity controls the anisotropy of focal adhesions. *Proc. Natl. Acad. Sci. USA.* 101:12520–12525.

23. Bruinsma, R. 2005. Theory of force regulation by nascent adhesion sites. *Biophys. J.* 89:87–94.

24. Bershadsky, A., M. Kozlov, and B. Geiger. 2006. Adhesion-mediated mechanosensitivity: a time to experiment, and a time to theorize. *Curr. Opin. Cell Biol.* 18:472–481.

25. Elosegui-Artola, A., R. Oria, …, P. Roca-Cusachs. 2016. Mechanical regulation of a molecular clutch defines force transmission and transduction in response to matrix rigidity. *Nat. Cell Biol.* 18:540–548.

26. Wu, Z., S. V. Plotnikov, …, J. Liu. 2017. Two distinct actin networks mediate traction oscillations to confer focal adhesion mechanosensing. *Biophys. J.* 112:780–794.

27. Zhang, X., G. Jiang, …, M. P. Sheetz. 2008. Talin depletion reveals independence of initial cell spreading from integrin activation and traction. *Nat. Cell Biol.* 10:1062–1068.

28. Atherton, P., B. Stutchbury, …, C. Ballestrem. 2015. Vinculin controls talin engagement with the actomyosin machinery. *Nat. Commun.* 6:10038.

29. Humphries, J. D., P. Wang, …, C. Ballestrem. 2007. Vinculin controls focal adhesion formation by direct interactions with talin and actin. *J. Cell Biol.* 179:1043–1057.

30. Thievessen, I., P. M. Thompson, …, C. M. Waterman. 2013. Vinculin-actin interaction couples actin retrograde flow to focal adhesions, but is dispensable for focal adhesion growth. *J. Cell Biol.* 202:163–177.

31. Johnson, R. P., and S. W. Craig. 1995. F-actin binding site masked by the intramolecular association of vinculin head and tail domains. *Nature.* 373:261–264.

32. Goult, B. T., X. P. Xu, …, D. Hanein. 2013. Structural studies on full-length talin1 reveal a compact auto-inhibited dimer: implications for talin activation. *J. Struct. Biol.* 184:21–32.

33. Sun, Z., H. Y. Tseng, …, R. Fässler. 2016. Kank2 activates talin, reduces force transduction across integrins and induces central adhesion formation. *Nat. Cell Biol.* 18:941–953.

34. Cohen, D. M., H. Chen, …, S. W. Craig. 2005. Two distinct head-tail interfaces cooperate to suppress activation of vinculin by talin. *J. Biol. Chem.* 280:17109–17117.

35. Goult, B. T., T. Zacharchenko, …, I. L. Barsukov. 2013. RIAM and vinculin binding to talin are mutually exclusive and regulate adhesion assembly and turnover. *J. Biol. Chem.* 288:8238–8249.

36. Austen, K., P. Ringer, …, C. Grashoff. 2015. Extracellular rigidity sensing by talin isoform-specific mechanical linkages. *Nat. Cell Biol.* 17:1597–1606.

37. Kumar, A., M. Ouyang, …, M. A. Schwartz. 2016. Talin tension sensor reveals novel features of focal adhesion force transmission and mechanosensitivity. *J. Cell Biol.* 213:371–383.

38. Galbraith, C. G., K. M. Yamada, and M. P. Sheetz. 2002. The relationship between force and focal complex development. *J. Cell Biol.* 159:695–705.

39. Saunders, R. M., M. R. Holt, …, D. R. Critchley. 2006. Role of vinculin in regulating focal adhesion turnover. *Eur. J. Cell Biol.* 85:487–500.

40. Dumbauld, D. W., T. T. Lee, …, A. J. García. 2013. How vinculin regulates force transmission. *Proc. Natl. Acad. Sci. USA.* 110:9788–9793.

41. Grashoff, C., B. D. Hoffman, …, M. A. Schwartz. 2010. Measuring mechanical tension across vinculin reveals regulation of focal adhesion dynamics. *Nature.* 466:263–266.

42. Case, L. B., M. A. Baird, …, C. M. Waterman. 2015. Molecular mechanism of vinculin activation and nanoscale spatial organization in focal adhesions. *Nat. Cell Biol.* 17:880–892.

43. del Rio, A., R. Perez-Jimenez, …, M. P. Sheetz. 2009. Stretching single talin rod molecules activates vinculin binding. *Science.* 323:638–641.

44. Hirata, H., H. Tatsumi, …, M. Sokabe. 2014. Force-dependent vinculin binding to talin in live cells: a crucial step in anchoring the actin cytoskeleton to focal adhesions. *Am. J. Physiol. Cell Physiol.* 306:C607–C620.

45. Atherton, P., B. Stutchbury, …, C. Ballestrem. 2016. Mechanosensitive components of integrin adhesions: role of vinculin. *Exp. Cell Res.* 343:21–27.

46. Yao, M., B. T. Goult, …, J. Yan. 2014. Mechanical activation of vinculin binding to talin locks talin in an unfolded conformation. *Sci. Rep.* 4:4610.

47. Carisey, A., R. Tsang, …, C. Ballestrem. 2013. Vinculin regulates the recruitment and release of core focal adhesion proteins in a force-dependent manner. *Curr. Biol.* 23:271–281.

48. Wolfenson, H., A. Bershadsky, …, B. Geiger. 2011. Actomyosin-generated tension controls the molecular kinetics of focal adhesions. *J. Cell Sci.* 124:1425–1432.

49. Lavelin, I., H. Wolfenson, …, B. Geiger. 2013. Differential effect of actomyosin relaxation on the dynamic properties of focal adhesion proteins. *PLoS One.* 8:e73549.

50. Lele, T. P., J. Pendse, …, D. E. Ingber. 2006. Mechanical forces alter zyxin unbinding kinetics within focal adhesions of living cells. *J. Cell. Physiol.* 207:187–194.

51. Stutchbury, B., P. Atherton, …, C. Ballestrem. 2017. Distinct focal adhesion protein modules control different aspects of mechanotransduction. *J. Cell Sci.* 130:1612–1624.

52. Mierke, C. T., P. Kollmannsberger, …, B. Fabry. 2010. Vinculin facilitates cell invasion into three-dimensional collagen matrices. *J. Biol. Chem.* 285:13121–13130.

53. Cohen, D. M., B. Kutscher, …, S. W. Craig. 2006. A conformational switch in vinculin drives formation and dynamics of a talin-vinculin complex at focal adhesions. *J. Biol. Chem.* 281:16006–16015.

54. Rothenberg, K. E., S. S. Neibart, …, B. D. Hoffman. 2015. Controlling cell geometry affects the spatial distribution of load across vinculin. *Cell. Mol. Bioeng.* 8:364–382.

55. Chen, H., H. L. Puhl, III, …, S. R. Ikeda. 2006. Measurement of FRET efficiency and ratio of donor to acceptor concentration in living cells. *Biophys. J.* 91:L39–L41.

56. LaCroix, A. S., K. E. Rothenberg, …, B. D. Hoffman. 2015. Construction, imaging, and analysis of FRET-based tension sensors in living cells. *Methods Cell Biol.* 125:161–186.

57. Zamir, E., B. Z. Katz, …, Z. Kam. 1999. Molecular diversity of cell-matrix adhesions. *J. Cell Sci.* 112:1655–1669.

58. Wehrle-Haller, B. 2007. Analysis of integrin dynamics by fluorescence recovery after photobleaching. *Methods Mol. Biol.* 370:173–202.

59. Chen, H., D. M. Cohen, …, S. W. Craig. 2005. Spatial distribution and functional significance of activated vinculin in living cells. *J. Cell Biol.* 169:459–470.

60. Majumdar, Z. K., R. Hickerson, …, R. M. Clegg. 2005. Measurements of internal distance changes of the 30S ribosome using FRET with multiple donor-acceptor pairs: quantitative spectroscopic methods. *J. Mol. Biol.* 351:1123–1145.

61. Jurchenko, C., and K. S. Salaita. 2015. Lighting up the force: investigating mechanisms of mechanotransduction using fluorescent tension probes. *Mol. Cell. Biol.* 35:2570–2582.

62. Gayrard, C., and N. Borghi. 2016. FRET-based molecular tension microscopy. *Methods.* 94:33–42.

63. Thompson, P. M., C. E. Tolbert, …, S. L. Campbell. 2014. Identification of an actin binding surface on vinculin that mediates mechanical cell and focal adhesion properties. *Structure.* 22:697–706.

64. Diez, G., V. Auernheimer, …, W. H. Goldmann. 2011. Head/tail interaction of vinculin influences cell mechanical behavior. *Biochem. Biophys. Res. Commun.* 406:85–88.

65. Sarangi, B. R., M. Gupta, …, B. Ladoux. 2017. Coordination between intra- and extracellular forces regulates focal adhesion dynamics. *Nano Lett.* 17:399–406.

66. Pasapera, A. M., I. C. Schneider, …, C. M. Waterman. 2010. Myosin II activity regulates vinculin recruitment to focal adhesions through FAK-mediated paxillin phosphorylation. *J. Cell Biol.* 188:877–890.

67. Auernheimer, V., L. A. Lautscham, …, W. H. Goldmann. 2015. Vinculin phosphorylation at residues Y100 and Y1065 is required for cellular force transmission. *J. Cell Sci.* 128:3435–3443.

68. Yamashita, H., T. Ichikawa, …, N. Kioka. 2014. The role of the interaction of the vinculin proline-rich linker region with vinexin α in sensing the stiffness of the extracellular matrix. *J. Cell Sci.* 127:1875–1886.

69. Riedl, J., A. H. Crevenna, …, R. Wedlich-Soldner. 2008. LifeAct: a versatile marker to visualize F-actin. *Nat. Methods.* 5:605–607.

70. Rahman, A., S. P. Carey, …, C. A. Reinhart-King. 2016. Vinculin regulates directionality and cell polarity in 2D, 3D matrix and 3D microtrack migration. *Mol. Biol. Cell.* 27:1431–1441.

71. Thievessen, I., N. Fakhri, …, B. Fabry. 2015. Vinculin is required for cell polarization, migration, and extracellular matrix remodeling in 3D collagen. *FASEB J.* 29:4555–4567.

72. Huang, D. L., N. A. Bax, …, A. R. Dunn. 2017. Vinculin forms a directionally asymmetric catch bond with F-actin. *Science.* 357:703–706.

73. Dmitrieff, S., and F. Nédélec. 2016. Amplification of actin polymerization forces. *J. Cell Biol.* 212:763–766.

74. Golji, J., and M. R. Mofrad. 2013. The interaction of vinculin with actin. *PLoS Comput. Biol.* 9:e1002995.

75. Sun, L., J. K. Noel, …, J. N. Onuchic. 2017. Molecular simulations suggest a force-dependent mechanism of vinculin activation. *Biophys. J.* 113:1697–1710.

76. Roca-Cusachs, P., A. del Rio, …, M. P. Sheetz. 2013. Integrin-dependent force transmission to the extracellular matrix by α-actinin triggers adhesion maturation. *Proc. Natl. Acad. Sci. USA.* 110:E1361–E1370.

77. Le, S., X. Hu, …, J. Yan. 2017. Mechanotransmission and mechanosensing of human alpha-actinin 1. *Cell Reports.* 21:2714–2723.

78. Kong, F., A. J. García, …, C. Zhu. 2009. Demonstration of catch bonds between an integrin and its ligand. *J. Cell Biol.* 185:1275–1284.